


ARTICLE

<https://doi.org/10.1038/s42005-020-0296-4>

OPEN

Giant localised spin-Peltier effect due to ultrafast domain wall motion in antiferromagnetic metals

R.M. Otxoa^{1,2*}, U. Atxitia³, P.E. Roy¹ & O. Chubykalo-Fesenko⁴ 

Spin thermo-electric phenomena have attracted wide attention recently, e.g., the spin Peltier effect—heat generation by magnonic spin currents. Here, we find that the spin Peltier effect also manifests as a heat wave accompanying fast moving magnetic textures. High speed and extreme magnetic excitation localisation are paramount for efficient transfer of energy from the spin-degrees of freedom to electrons and lattice. While satisfying both conditions is subject to severe restrictions in ferromagnets, we find that domain walls in antiferromagnets can overcome these limitations due to their ultrahigh mobility and ultra-small widths originating from the relativistic contraction. To illustrate our findings, we show that electric current driven domain wall motion in the antiferromagnetic metal Mn_2Au can carry a localised heat wave with temperature up to 1 K. Since domain walls are localised magnetic objects, this effect has the potential for nanoscale heating sensing and functionalities.

¹Hitachi Cambridge Laboratory, J. J. Thomson Avenue, Cambridge CB3 0HE, United Kingdom. ²Donostia International Physics Center, Donostia San Sebastian 20018, Spain. ³Dahlem Center for Complex Quantum Systems and Fachbereich Physik, Freie Universität Berlin, 14195 Berlin, Germany. ⁴Instituto de Ciencia de Materiales de Madrid, CSIC, Cantoblanco, 28049 Madrid, Spain. *email: ro274@cam.ac.uk

Heat production in electronics constitutes one of the major problems of the ever-growing information technology society and is a source of energy waste. To convert this waste to useful green house technologies is a primary societal challenge and a research there is doing its first steps. For instance, nanoscale heating has become crucial for the existence of several emerging non-disruptive technologies, from cancer treatments, to information technologies such as heat assisted magnetic recording¹. Still, it remains a challenge to find ways not only to control the level of heating but also to do it in a fast, energy-efficient manner at ever decreasing length scales. Spin thermophysics offer a wide plethora of phenomena to be exploited at the nanoscale, such as the Spin Seebeck² and its inverse the spin Peltier effect (SPE)^{3,4}, i.e., the generation of thermal gradients with spin currents. The experimental demonstration of the SPE has become possible only recently based on the idea that spin currents passing through a magnetic texture would heat one end and cool down the other, thereby creating a thermal gradient^{3,4}. At the same time, ultrafast manipulation and control of spin degrees of freedom is possible by the use of femtosecond laser pulses⁵, and picosecond electric currents⁶, and hold the promise to transform information technology. Electrically driven domain walls (DWs) in antiferromagnets (AFMs) are also known to achieve velocities proper for ultrafast magnetisation dynamics. Here, combining theoretical insights from the fields of spin thermophysics, ultrafast spin dynamics and antiferromagnetic spintronics we demonstrate the possibility of localised giant SPE by high-speed motion of AFM DWs.

In terms of using high speed and localised magnetic textures, the idea of racetrack memory architecture, as proposed for fast, high density 3D magnetic memories is very useful. Race track memory concepts are based on moving textures, such as domain walls⁷ or skyrmions⁸, localised to move within the confines of a magnetic track. The feasibility of ultrafast race-track memories calls for the use of antiferro or ferri-magnetic systems^{9–12}. Antiferromagnets represent one of the most promising candidates in the quest for faster, energy efficient technologies^{13–15}. Theoretically, the velocity in antiferromagnetic textures is not limited by the so called Walker breakdown^{16,17}, and can potentially achieve tens of km/s^{10,18}, in direct comparison to hundreds of m/s in their ferromagnetic counterpart. Since antiferromagnets are robust against magnetic fields, electric currents have been proposed as an alternative way to control and manipulate AFM spin dynamics, from domain wall motion^{18,19} to magnetic switching⁹. However, the absence of net magnetic moment makes them challenging to probe reliably.

We demonstrate the possibility to use electrically driven AFM DW motion to generate a significant localised heat wave, with a transient electronic temperature rise at least three orders of magnitude larger than in the ferromagnetic case. To further control and exploit the predicted giant- SPE, it is crucial to understand the means by which the spin dynamics dissipates energy into the surroundings in the whole range of time and length scales. Notably, by developing a kinetic model where both local and non-local electron, phonon and spin relaxation are included, we are able to identify relevant timescales and extend the existing framework for the AFM DW dynamics onto the case of non-equilibrium ultrafast dynamics.

This approach enables us to reveal that the magnetic energy transfer takes place in the previously unexplored subpicosecond time scale. This creates an imbalance between the heated electrons and the colder lattice. Subsequently, those hot electrons release their excess energy to the lattice via electron–phonon coupling, a thermalisation process that takes several picoseconds. Finally, lateral heat diffusion transports thermal energy away from the DW position in the hundred picosecond scale.

Concerning the use of AFM in nanoheating technologies, the standard way of applying cyclic magnetic fields would hardly work due to the small coupling owing to their vanishing net magnetisation. However, relatively low electric currents are able to drive the DWs in AFMs up to their maximum velocity, determined by the magnon group velocity (see Supplementary Note 1), which lies in the elusive range of THz. In that ultrafast spin dynamical regime, two effects emerge which need to be considered; (i) Lorentz contraction of the characteristic lengths due to the relativistic nature of AFM spin dynamics, and (ii) ultrafast magnetic energy conversion into heat. While the former has been investigated in literature for some classes of AFMs²⁰, the latter effect remains largely unknown. In this work, we reveal the fundamental role of the ultra-high speeds and Lorentzian contraction of DW dynamics in the magnetic energy conversion into dissipation of a moving AFM magnetic texture.

In terms of viable materials for this approach, anti-ferromagnetic metals would appear to be favoured over counterpart insulators since in the latter the magnetic energy would be absorbed into the magnon bath rather than transferred to the electronic degrees of freedom²¹. Moreover, magnon relaxation in insulators is a slow process, which could be comparable to the thermal diffusion. In metals however, spin degrees of freedom efficiently couple to the electronic system²². This results for example in femtosecond (10^{-15} s) time scale dynamics of spins, electrons and lattice²³, opening the door to Petahertz (10^{15} s⁻¹) spintronics²⁴. This strong coupling between the spin, electrons and lattice provides an ideal benchmark for the possibility of ultrafast energy transfer from spin to the electron system by pure high-speed DW dynamics in AFM metals.

Results

Heat generation due to an AFM DW moving at high speeds.

The response of a magnet to an external stimulus strongly depends on the way dissipation takes place, which in turn controls the magnetic response in processes such as DW motion, switching and spin transport. The dynamics of the angular momentum dissipation in magnets is well described by the Gilbert relaxation term in the Landau-Lifshitz-Gilbert equation of motion where the relaxation rate is proportional to the so-called Gilbert damping, α . This is connected to the magnetic energy dissipation described by the Rayleigh dissipation functional, $\dot{Q}_{\text{DW}} = \int dV \eta \dot{\mathbf{S}}^2(\mathbf{r})$, where $\eta = \mu_{\text{at}}\alpha/\gamma$, γ is the gyromagnetic ratio and μ_{at} is the sublattice atomic moment per unit volume. We use the Rayleigh dissipation functional to estimate the temperature rise while the DW is moving.

Within the Lagrangian formalism for a stationary moving (along x -direction) 1D DW in a layered AFM (or a ferromagnet), the Rayleigh dissipation function (per atomic spin) can be derived as (see Supplementary Note 2)

$$\dot{Q}_{\text{DW}}(x, t) = \frac{\mu_{\text{at}}}{\gamma} \alpha \left(\frac{v_{\text{DW}}}{\Delta_{\text{DW}}} \right)^2 \frac{1}{\cosh^2(q)}, \quad (1)$$

where $q = (x - v_{\text{DW}}t)/\Delta_{\text{DW}}$, v_{DW} is the DW velocity and Δ_{DW} is the DW width. For a stationary moving DW in the absence of thermal diffusion and other energy transfer terms, the temperature profile accompanying the DW propagation can be estimated as

$$\Delta T(x, t) = \frac{2}{C} \frac{\mu_{\text{at}}}{\gamma} \alpha \frac{v_{\text{DW}}}{\Delta_{\text{DW}}} \tanh(q). \quad (2)$$

where C is the electron (phonon) bath heat capacity. We note that the temperature rise scales with the ratio $v_{\text{DW}}/\Delta_{\text{DW}}$, which is advantageous for an AFM DW due to the Lorentz contraction of Δ_{DW} down to the atomic limit, and the possibility to achieve

magnonic velocities (see Supplementary Note 2 and Supplementary Movie 1). Equation (2) accounts for a direct and instantaneous heating of the electron system by a moving DW. Important remaining questions are: what is the time scale of such energy transfer from the DW motion to the electron bath? what is the impact of the electron-phonon coupling and thermal diffusion on the temperature dynamics? To answer these questions, we explore the non-equilibrium (non steady) DW dynamics in the metallic AFM, Mn_2Au , driven by spin-orbit fields in a track and its impact on the track temperature.

Efficient DW motion can be achieved in certain AFM metals by injecting electric currents into them. In particular, in crystals with locally broken inversion symmetry the magnetic sites A and B form inversion partners. Upon passing an electrical current along the basal planes, the inverse spin galvanic effect produces a staggered local spin accumulation with opposite polarities. The effect of the current is then to produce a local staggered spin-orbit (SO) field which is perpendicular to the spin-polarised current direction and is linearly proportional to its magnitude. The torque generated on each AFM sub-lattice has, therefore, the same form as in ferromagnets. Together with the AFM metal CuMnAs , Mn_2Au is one of the few AFM materials with high enough critical temperature (1500 K), and the required crystal symmetry. This makes it suitable for spintronic applications. Moreover, recent estimations of the effective SO fields, B^{SO} are ~ 2 mT per 10^7 A/cm 2 (slightly lower than for CuMnAs)⁹.

For the description of the energetics of Mn_2Au we consider a classical spin Hamiltonian (See Methods). Within this model, the Mn spins are responsible for the magnetic properties. The electrically driven DW dynamics is calculated by means of computer simulations based on atomistic spin dynamics²⁵ using the solution of the Landau-Lifshitz-Gilbert (LLG) equations on a discrete lattice. A moving DW is characterised by its instantaneous position and velocity of its centre, (q, v_{DW}) (see Fig. 1a). In AFMs, the Lorentz contraction means that the width Δ_{DW} of the DW depends on v_{DW} and is limited by the maximum magnon group velocity v_g , i.e., $\Delta_{\text{DW}} = \Delta_0 \sqrt{1 - (v_{\text{DW}}/v_g)^2}$ where Δ_0 is the DW width at rest. An electric current passing through Mn_2Au creates a staggered spin-orbit torque with the corresponding field B^{SO} which drives the DW at a velocity, $v_{\text{DW}} = (\gamma/\alpha)B^{\text{SO}}\Delta_{\text{DW}}$. Due to energy conservation, a stationary moving DW dissipates energy into the medium at the same rate as the Zeeman energy lowers due to the domain switching. The dynamics of the redistribution of this excess of energy into the different subsystems is the main result of this work.

Atomic spin dynamics simulations (ASD) permit us to calculate $S_i(t)$, and consequently $q(t)$, $v_{\text{DW}}(t)$ and $\Delta_{\text{DW}}(t)$ are obtained. Those time-dependent quantities are then fed into Eq. (1) to calculate the instantaneous local $\dot{Q}_{\text{DW}}(\mathbf{r}_i, t)$. This quantity enters into the equation of motion for the electron and lattice temperature dynamics, which is described by the two temperature model discussed in Methods section. Figure 1b depicts the transient dynamics of the local electron and phonon temperature profiles due to a high speed moving DW. The electron temperature shows a peak temperature lagging slightly behind the DW centre. At the same time the phonon temperature shows a much smoother profile, owing to the indirect coupling to the heat source (moving DW) via the electron system, (G_{e-ph}) . The heat wave is well localised around the centre of the DW. The excess of energy in the electronic system is rapidly transferred to the lattice via the electron-phonon coupling at characteristic timescales of the order ~ 1 ps. At the same time, lateral heat transport is also present, flow of energy from hot to cold regions. Additionally, the created temperature gradient can produce the feedback phenomenon of the DW retardation via the

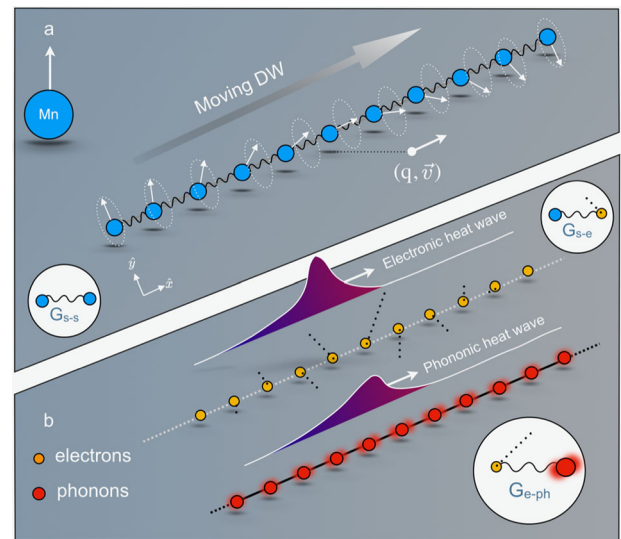


Fig. 1 Spin dynamics, and electron and phonon energy dynamics. **a** In Mn_2Au the ions of Mn provide the spins (white arrows). Two magnetic domains are separated by a moving domain wall (DW), defined by its position and velocity (q, v) . **b** Subpicosecond heat dissipation is provided via coupling of the spins' degrees of freedom located at the DW to the electrons defined by G_{s-e} . This creates a localised heat wave of hot electrons which accompanies the moving DW. These hot electrons are now in non thermal equilibrium with the lattice, described by a phonon temperature. The electron-phonon coupling, G_{e-ph} , is responsible for the heat transfer from the hot electrons to the colder phonons. This process thermalises the electron and phonon system to a final common temperature.

spin-Seebeck effect which tendency is to push the DW to a hotter region, lagging behind the DW centre. Our estimations show that this effect is at least 100 times smaller than that of the current (see details in the Supplementary Note 3).

We should note that additional channels of energy conversion also exist. For instance, magnon creation, which in turn can transport energy away from the heat source. In our simulations we do not see significant spin wave creation, probably due to the conditions we are assuming here: low temperature and 15 ps linear ramp time of driving current as opposed to a square pulse which lead to a steady DW motion. However, our model is sufficiently general and in the future we can consider situations where the magnon creation effect is important. One of this scenario is the domain walls collision where we expect strong magnon generation and high energy release. Furthermore, we neglect the Joule heating contribution in our model, although its contribution may be larger²⁶ than that related to the DW motion via the spin-Peltier effect. Our estimations show that for Mn_2Au grown on the MgO the temperature increase during the action of the 4 pulses considered here is around 7.5 K (see details in the Supplementary Note 4). However, the Joule heating only provides a homogeneous background. We hope that these effects would be possible to distinguish by proper calibration in the real experimental set up.

In our simulations, we start by injecting an electric current with the time profile illustrated in Fig. 2a; (A \rightarrow B) electric current with a rising time of 15 ps up to a peak value of $B^{\text{SO}}(t) = 60$ mT. The value of B^{SO} is kept constant for the following 5 ps (closed green circles in Fig. 2a) before reducing it to zero (B \rightarrow C), with a falling time of 15 ps and for 3.5 ps (closed purple circles in Fig. 2a). This time pattern of the electric current moves the AFM DW from the left to right of the track. This is represented in the outset of Fig. 2a by the blue arrow at the DW profile. In

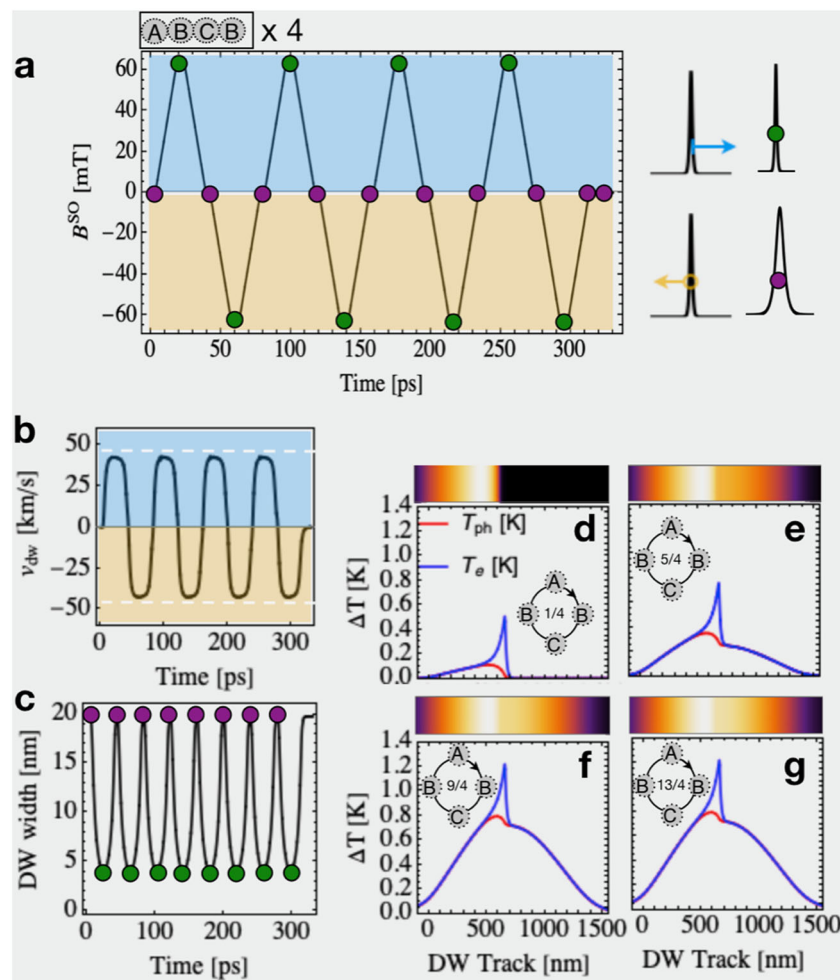


Fig. 2 Dynamics of the domain wall driven by spin-orbit fields generated by electric currents. **a** Time dependence of the spin orbit field, $B^{SO}(t)$. **b** Time resolved domain wall (DW) velocity, dashed red lines correspond to v_g , the maximum magnon group velocity. **c** Time resolved DW width, Δ_{DW} , where purple dots indicate time moments when Δ_{DW} is maximum, which corresponds to minimum domain wall velocity, v_{DW} (see panel **b**). Green dots indicate time moments when Δ_{DW} is minimum (maximum v_{DW}). **d-g** Spatial-temporal snapshots of the temperature dynamics $\Delta T(t)$ in the sample region where the DW moves, corresponding to the time moments **(d)** 1/4 of the period **(e)** 5/4 of the period **(f)** 9/4 of the period **(g)** 13/4 of the period.

particular, from **A** to **B** the DW is accelerated up to approximately its maximum velocity, ($v_{DW} \approx v_g$) (Fig. 2b). In our simulations, we repeat this time pattern for the electric current (**A** → **B** → **C**) but with opposite electric current direction, which effectively means negative values of B^{SO} and consequently the DW moves into the opposite direction, from the right to the left, represented in the outset of Fig. 2a by the yellow arrow on top of the DW profile.

The dissipated heat input rate from DW into the electron system scales with the ratio, $\dot{Q}_{DW-e} \sim (v_{DW}/\Delta_{DW})^2$. From ASD simulations of the AFM DW motion we gain information about the dynamics of the DW velocity, v_{DW} (Fig. 2b) as well as the DW width, Δ_{DW} (Fig. 2c). During the rise-time of $B^{SO}(t)$ (**A** → **B** in Fig. 2a), the DW velocity increases almost up to v_g relatively quick, related to the non-linear dependence of $v_g(B^{SO}(t))$. The temporal pattern of the DW velocity approximates to a step function with $v_{DW} \approx v_g$ (dashed white line in Fig. 2b). In each half-cycle DW displaces around 1400 nm in only 37.5 picoseconds, that is it, a mean DW velocity is of $\langle v_{DW} \rangle = 33.15$ km/s. This value is close to the maximum velocity the DW achieved in our simulations, $v_{DW}^{max} = 43.3$ km/s extracted from the dispersion relation (See Supplementary Note 1). The same process is repeated with negative values of B^{SO} , thus, the DW repeats the dynamics described before and returns to

the initial position. This periodic cycling is repeated 4 times in our computer simulations. We note here that the necessary ingredient to achieve large amounts of dissipated power is not only high-speed DW velocity but also an extremely small DW width. Antiferromagnetic DWs are ideal for these conditions to be fulfilled, due to the absence of Walker breakdown—upon which the domain wall deforms, resulting in a reduction of its velocity—and ultra-small DW widths when the DW moves at high speeds. In our simulations, the DW width Δ_{DW} periodically shrinks and expands comprising values from circa 20 nm (closed purple circles in Fig. 2c) down to circa 4 nm (closed green circles in Fig. 2c). This behaviour makes that at the centre of track, where v_{DW} is maximum and Δ_{DW} is minimum, the maximum temperature rise is achieved.

One of our main results is the detailed description of the distinct spatial-temporal dynamics of the temperature increase of both, the electrons, ΔT_e , and the phonons, ΔT_{ph} , in the sample region where the DW moves (Fig. 2d-g). A snapshot at **B** (Fig. 2a) of the spatial profile of ΔT_e and ΔT_{ph} in the track shows the existence of electronic and phonon localised heat waves with an electronic peak temperature at the DW position (Fig. 2d). Interestingly, ΔT_e and ΔT_{ph} remain different during time scale determined by the electron-phonon relaxation time, $\tau_{e-ph} \approx G_{e-ph}/C_e \approx 1.2$ picoseconds for the parameters used here. One

can define the characteristic length scale for which the electron and phonon temperature are different, l_{e-ph} , by considering that the DW moves close to its maximum velocity, in this case, $l_{e-ph} = v_{DW}^{\max} \tau_{e-ph} \approx 48$ nm.

An important result of our findings is the estimation of the accumulated peak temperature in one driving-cycle, which reaches almost 0.8 K for our system parameters (Fig. 2e). As we have demonstrated before, the temperature increase scales as $\Delta T \sim v_{DW}/\Delta_{DW}$, thus the global maximum ΔT is located in the centre of the region of the DW movement where the DW velocity is maximum and the DW width is minimum. The evolution of the electron temperature rise at the centre of the track shows how the DW motion releases magnetic energy into the electron system in time scale of subpicoseconds, with peak electron temperature appearing only a few hundreds of femtoseconds after the DW passes. This excess of energy is thereafter transferred to the phonon system via electron-phonon coupling in time scale of the order of the picosecond. From our simulations we also observe that the lateral diffusion is not fast enough to delocalise the heat wave, even though we have considered a relatively large thermal conductivity corresponding to a metal. Once the DW has passed, lateral thermal diffusion sets in with time scale of the order of hundreds of picoseconds. For length scales away from the domain wall position the electron and phonon temperatures are already in thermal equilibrium. These timescales are much shorter than the expected timescale for the energy equilibration with the outside world (the air, for example).

We discuss now the total heat dissipated in our system per cycle (Fig. 3a). Our excitation protocol produces a phonon heat accumulation at the track centre. In terms of the phonon (electron) temperature the value of 1 K is reached already in 300 ps (Fig. 3b) with 4 field cycles with a full width at half maximum of 1 micrometre (Fig. 3a). The rapid accumulation is possible due to the high-speed character of the AFM DWs. At this timescales the heat transfer to the outside media is expected to be small so that a giant magnetocaloric effect is induced.

Discussion

The described above phenomena open the door to control heating at the nanoscale in a fast manner. It is worth discussing the differences and similarities between the heating process by AFM DW and that of ferromagnetic nanoparticles performing coherent magnetisation rotation induced by external oscillating magnetic

fields. The latter is a standard way to heat, for example, tumour cells in magnetic hyperthermia treatment. Energetic considerations show that the magnetic energy density release is different to zero for irreversible processes only, and is equal to the hysteresis loop area, $\Delta\epsilon = \int M(B)dB$, where M is the magnetisation. In the absence of other heat losses, one can estimate the maximum temperature rise as $\Delta T \sim \Delta\epsilon/C$ where C is the heat capacity. Although useful, this argument can produce an impression that a relatively large temperature rise can be achieved by only increasing the applied magnetic field. The real situation is, however, more complex since dynamical considerations need to be taken into account. Specifically, the rotational speed is in the nanoseconds range, i.e. the maximum possible heat will correspond to fields with the magnitude of the coercive field applied at frequencies smaller than GHz. This timescale is much slower than the AFM dynamics considered here. Faster field cycling implies minor hysteresis loops leading to a huge decrease of the heating output. Additionally, at this timescale, the interface heat transfer (to the outside media) is very efficient which is in contrast to our case. For comparison, simple estimations show that a small magnetite nanoparticle of 10 nm diameter, under the best conditions of major hysteresis loop would produce heat of the order of 10 mK per field cycle. This estimation is 2-3 orders of magnitude lower than our calculations for AFM DW motion.

We note that for commonly used ferromagnetic materials, heating by moving DWs would not be so efficient as in AFM. For example, for standard parameters of permalloy, we estimate that the DW motion can carry electron temperature pulses of a maximum of 1 mK. Thermal diffusion also plays an important role in the delocalisation of the temperature rise in this case. The heat diffusion rate is defined by the parameter $\eta = D/v_{DW}\Delta_{DW}$ where $D = k_e/C_e$ is the electron thermal conductivity. If this parameter is large, thermal diffusion efficiently takes temperature away during the DW motion. Considering the typical metal value $D = 10^{-4}$ m²/s, the above parameter $\eta \gg 1$ for permalloy and $\eta < 1$ for Mn₂Au. Thus the negligible heat wave accompanying the permalloy DW will be completely delocalised, whereas for Mn₂Au it is localised at the DW.

Importantly, since eventually heat will spread all over the sample, the particular dynamics of the relaxation of the localised temperature rise is paramount for devising experiments and devices able to exploit this new concept, we present here. The effect hinges to the field of ultrafast spin caloritronics fostered by the recent demonstration of subpicosecond spin Seebeck effect²⁷.

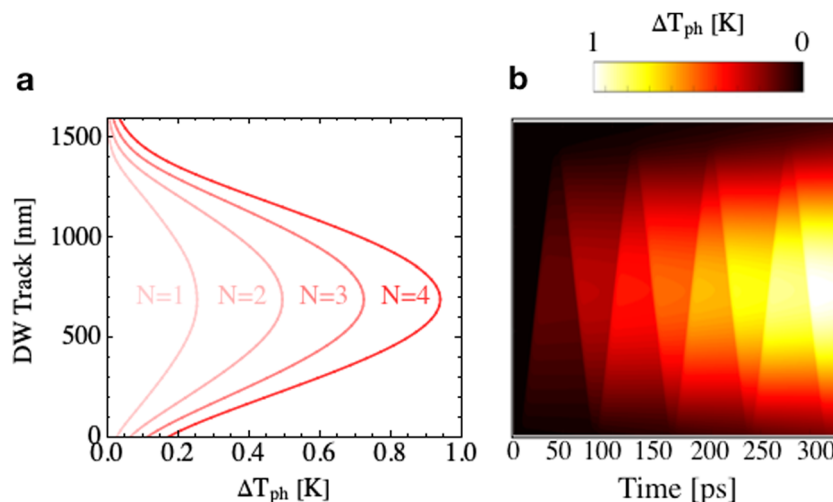


Fig. 3 Heat accumulation in the stripe. **a** Spatial distribution of the phonon temperature increase ΔT_{ph} after each cycle of the spin-orbit field, $N = 1, 2, 3$, and 4. **b** Spatial-temporal evolution of the accumulated temperature increase in the phonon system.

Along this line, it remains a challenge to drive AFM DWs into magnonic velocities, and to develop experimental techniques in order to detect DW dynamics at these ultrafast timescales. Notably, we believe that nanoscale confined heating at the domain wall position can be used to track the DW position and velocity by measuring the temperature increase with, for example, scanning thermal microscopy. Recent reports indicate that by using the anomalous Nerst effect, thermal nanoscale detection of the DW motion (although in the timescale much larger than our) is possible²⁸. Finally, the localised phonon temperature increase will create phonon waves, which might be possible to measure in a similar manner as in the reported ultrafast Einstein-de Haas effect²³.

In some sense the heat production of electrically driven DW motion is analogous to the Joule heating, when passing an electric current through a resistive material. In our case, the role of the moving electrons is played by the DW, which implies that the mechanisms of energy conversion into heat occur at the site of the DW. This enables a highly localised heat wave source, provided that the DW moves faster than typical diffusion processes, with the added benefit of the heat source being movable.

Interestingly, the spin-Peltier effect, reported here, is not restricted to moving DWs in AFMs but is a universal characteristic of magnetic textures moving at high velocities. Therefore, the concept can be extended to other textures, such as skyrmions or vortices. As an example, DWs in cylindrical nanowires and nanotubes also lack the Walker breakdown phenomenon and reach velocities similar to those considered here²⁹. Systems with perpendicular anisotropy and Dzyaloshinski-Moriya interactions³⁰ or ferrimagnets close to the angular momentum compensation point³¹ may also be good candidates to observe the predicted effect. However, the AFM has additional advantage of very small DW width, due to Lorentz contraction at high velocities, which can be reached using SO torques with reasonable current intensities.

Methods

Atomistic spin dynamics. The domain wall dynamics are solved on a spin-atomic cell structure of Mn₂Au. The computational domain is 60,000 cells long, one cell wide with periodic boundaries along the width and one cell thick. The total energy is described with the following atomistic classical spin Hamiltonian,

$$\begin{aligned} \mathcal{H} = & - \sum_{i \neq j} J_{ij} \mathbf{S}_i \cdot \mathbf{S}_j - K_{2\perp} \sum_i (\mathbf{S}_i \cdot \mathbf{u}_3)^2 - K_{2\parallel} \sum_i (\mathbf{S}_i \cdot \mathbf{u}_2)^2 \\ & - \frac{K_{4\perp}}{2} \sum_i (\mathbf{S}_i \cdot \mathbf{u}_3)^4 - \frac{K_{4\parallel}}{2} \sum_i (\mathbf{S}_i \cdot \mathbf{u}_1)^4 - \frac{K_{4\parallel}}{2} \sum_i (\mathbf{S}_i \cdot \mathbf{u}_2)^4 \quad (3) \\ & - \mu_s \sum_i \mathbf{S}_i \cdot \mathbf{B}_i^{\text{SO}}, \end{aligned}$$

where \mathbf{S}_i is a classical vector with $|\mathbf{S}_i| = 1$. The first term constitutes the exchange interaction between spins at sites i and j denoted by J_{ij} . The second term is a hard-axis magnetocrystalline anisotropy and terms three to five correspond to tetragonal magnetocrystalline anisotropy. The (unit) vectors \mathbf{u}_1 , \mathbf{u}_2 and \mathbf{u}_3 are directed along the axes of the Cartesian coordinate system used as detailed in the Supplementary Note 1. Finally the last term is the interaction between the magnetic moment and the staggered SO-field (where μ_s is the atomic moment). Material parameters used are the following: $J_{11} = -396k_B$, $J_{12} = -532k_B$, and $J_{13} = 115k_B$, where k_B is the Boltzmann constant. The atomic magnetic moment is set to $\mu_s = 4\mu_B$ (with μ_B being the Bohr magneton). Further, $K_{2\perp} = -1.3 \cdot 10^{-22}$ J, $K_{4\parallel} = 1.86 \cdot 10^{-25}$ J, $K_{4\perp} = 2K_{4\parallel}$ and $K_{2\parallel} = 7 \times K_{4\parallel}$. These parameters are the same as used in a previous work³².

The dynamics of the spins in Mn₂Au is described by a classical spin model framework based on the Landau-Lifshitz-Gilbert equation of motion

$$(1 + \alpha^2) \dot{\mathbf{S}}_i = -\gamma \mathbf{S}_i \times (\mathbf{B}_i^{\text{eff}} + \alpha \mathbf{S}_i \times \mathbf{B}_i^{\text{eff}}), \quad (4)$$

here, $\mathbf{B}_i^{\text{eff}} = -\frac{1}{\mu_s} \delta \mathcal{H} / \delta \mathbf{S}_i$, where \mathcal{H} is given in Equation (3). Here, α is the magnetic damping parameter, also known as Gilbert damping parameter. The gyromagnetic ratio is $\gamma = 1.76 \times 10^{11}$ (Ts)⁻¹. Similar to the Hamiltonian, the spin vectors are classical, constant length and normalised, $|\mathbf{S}_i| = 1$. In the presence of an electric current, the SO coupling creates an effective field, \mathbf{B}^{SO} , which is added to the

Table 1 Spin thermophysical parameters of Mn₂Au. Literature values for material parameters relevant for modelling the spin dynamics and heat transfer³³.

| Parameter | Value |
|--|--|
| Diffusion coefficient, k_e | 200 W/(Km) |
| electron heat capacity, $C_e = \gamma_e T_e$ | $\gamma_e = 10^3$ J/(m ³ K) |
| phonon heat capacity, C_{ph} | 1.5×10^6 J/(m ³ K) |
| electron-phonon coupling, $G_{e-\text{ph}}$ | 0.25×10^{18} W/(m ³ K) |
| Gilbert damping, α | 0.001 |

effective field, $\mathbf{B}_i^{\text{eff}}$. For further details concerning simulation procedure and data extraction, we refer to the Supplementary Note 1.

Two-temperature model. We use the two temperature model to describe the dynamics of the electron, T_e , and lattice, T_{ph} , temperatures, which for numerical purposes are discretised, providing local site-resolved temperatures $T_e(x, t)$ and $T_{\text{ph}}(x, t)$

$$C_e \frac{dT_e}{dt} = G_{e-\text{ph}}(T_e - T_{\text{ph}}) + k_e \frac{\partial^2 T}{\partial x^2} + \dot{Q}_{\text{DW}-e}(x, t) \quad (5)$$

$$C_{\text{ph}} \frac{dT_{\text{ph}}}{dt} = -G_{e-\text{ph}}(T_e - T_{\text{ph}}), \quad (6)$$

where C_e , C_{ph} are the electron and phonon specific heats, respectively and $\dot{Q}_{\text{DW}-e}(x, t)$ is defined by the energy input from the moving object. The coupling between electron and lattice systems is defined by the electron-phonon coupling constant, $G_{e-\text{ph}}$. Lateral heat transport is defined by $k_e \partial^2 T / \partial x^2$, where k_e is the electronic thermal conductivity. Exact values used in our model can be found in Table 1.

Data availability

The data generated for the current study are available from the corresponding author upon reasonable request.

Received: 6 August 2019; Accepted: 14 January 2020;

Published online: 06 February 2020

References

- Challenor, W. A. et al. Heat-assisted magnetic recording by a near-field transducer with efficient optical energy transfer. *Nat. Photon.* **3**, 220 (2009).
- Uchida, K. et al. Observation of the spin Seebeck effect. *Nature* **455**, 778 (2008).
- Daimon, S., Iguchi, R., Hioki, T., Saitoh, E. & Uchida, K.-I. Thermal Imaging of spin Peltier effect. *Nat. Commun.* **7**, 13754 (2016).
- Uchida, K.-I. et al. Combinatorial investigation of spin-orbit materials using spin Peltier effect. *Nature* **558**, 95 (2018).
- Kirilyuk, A., Kimel, A. V. & Rasing, T. Ultrafast optical manipulation of magnetic order. *Rev. Mod. Phys.* **82**, 2731 (2010).
- Yang, Y. et al. Ultrafast magnetization reversal by picosecond electrical pulses. *Sci. Adv.* **3**, e1603117 (2018).
- Parkin, S., Hayashi, M. & Thomas, L. Magnetic domain-wall racetrack memory. *Science* **320**, 190 (2008).
- Fert, A., Cros, V. & Sampaio, J. Skyrmions on the track. *Nat. Nanotechnol.* **8**, 152 (2013).
- Wadley, P. et al. Electrical switching of an antiferromagnet. *Science* **351**, 587–590 (2016).
- Yang, S.-H., Ryu, K.-S. & Parkin, S. Domain wall velocities of up to 750 m/s driven by exchange coupling torque in synthetic antiferromagnets. *Nat. Nanotechnol.* **10**, 221–226 (2015).
- Baltz, V. et al. Antiferromagnetic spintronics. *Rev. Mod. Phys.* **90**, 015005 (2018).
- Jungwirth, T. et al. The multiple directions of antiferromagnetic spintronics. *Nat. Phys.* **14**, 200–203 (2018).
- Barker, J. & Tretiakov, O. A. Static and dynamical properties of antiferromagnetic skyrmions in the presence of applied current and temperature. *Phys. Rev. Lett.* **116**, 147203 (2016).
- Thielemann-Kühn, N. et al. Ultrafast and energy-efficient quenching of spin order: antiferromagnetism beats ferromagnetism. *Phys. Rev. Lett.* **119**, 197202 (2017).

15. Olejník, K. et al. Terahertz electrical writing speed in an antiferromagnetic memory. *Sci. Adv.* **4**, eaar3566 (2018).
16. Schryer, N. L. & Walker, L. R. The motion of 180 domain walls in uniform dc magnetic fields. *J. Appl. Phys.* **45**, 5406 (1974).
17. Mougín, A., Cormier, M., Adam, J. P., Metaxas, P. J. & Ferre, J. Domain wall mobility, stability and Walker breakdown in magnetic nanowires. *Europhys. Lett.* **78**, 57007 (2007).
18. Gomonay, O., Jungwirth, T. & Sinova, J. High antiferromagnetic domain wall velocity induced by Néel spin-orbit torques. *Phys. Rev. Lett.* **117**, 017202 (2016).
19. Shiino, T. et al. Antiferromagnetic domain wall motion driven by spin-orbit torques. *Phys. Rev. Lett.* **117**, 087203 (2016).
20. Gomonay, E. V. & Loktev, V. M. Distinctive effects of a spin-polarized current on the static and dynamic properties of an antiferromagnetic conductor. *Low Temp. Phys.* **34**, 198 (2008).
21. Gomonay, O., Yamamoto, K. & Sinova, J. Spin caloric effects in antiferromagnets assisted by an external spin current. *J. Phys. D* **51**, 264004 (2018).
22. Bhattacharjee, N. et al. Néel spin-orbit torque driven antiferromagnetic resonance in Mn₂Au probed by time-domain THz spectroscopy. *Phys. Rev. Lett.* **120**, 237201 (2018).
23. Dornes, C. et al. The ultrafast Einstein-De Haas effect. *Nature* **565**, 209 (2019).
24. F. Siegrist et al. Petahertz Spintronics. arxiv:1812.07420 (2019).
25. Evans, R. F. L. et al. Atomistic spin model simulations of magnetic nanomaterials. *J. Phys. Cond. Mat.* **26**, 103202 (2014).
26. Meinert, M., Graulich, D. & Matalla-Wagner, T. Electrical switching of antiferromagnetic Mn₂Au and the role of thermal activation. *Phys. Rev. Appl.* **9**, 064040 (2018).
27. Seifert, T. S. et al. Femtosecond formation dynamics of the spin Seebeck effect revealed by terahertz spectroscopy. *Nat. Commun.* **9**, 2899 (2018).
28. Krzyszczyk, P. et al. Nanoscale thermoelectrical detection of magnetic domain wall propagation. *Phys. Rev. B* **95**, 220410(R) (2017).
29. Yan, M., Andreas, C., Kakay, A., Garcia-Sanchez, F. & Hertel, R. Fast domain wall dynamics in magnetic nanotubes: Suppression of Walker breakdown and Cherenkov-like spin wave emission. *Appl. Phys. Lett.* **99**, 122505 (2011).
30. Sethi, P. et al. Bi-directional high speed domain wall motion in perpendicular magnetic anisotropy Co/Pt double stack structures. *Sci. Rep.* **7**, 4964 (2017).
31. Kim, K. J. et al. Fast domain wall motion in the vicinity of the angular momentum compensation temperature of ferrimagnets. *Nat. Mat.* **16**, 1187 (2017).
32. Roy, P. E., Oetxoa, R. M. & Wunderlich, J. Robust picosecond writing of a layered antiferromagnet by staggered spin-orbit fields. *Phys. Rev. B* **94**, 014439 (2016).
33. Stojanovic, N., Maithripala, D. H. S., Berg, J. M. & Holtz, M. Thermal conductivity in metallic nanostructures at high temperature: Electrons, phonons, and the Wiedemann-Franz law. *Phys. Rev. B* **82**, 075418 (2010).

Acknowledgements

This work was partially supported by a STSM Grant from the COST Action CA17123. FU Berlin support by the Deutsche Forschungsgemeinschaft (DFG) through SFB/TRR 227 “Ultrafast Spin Dynamics”, Project A08 and the Spanish Ministry of Economy and Competitiveness under grants MAT2016-76824-C3-1-R and FIS2016-78591-C3-3-R are gratefully acknowledged.

Author contributions

R.M.O., U.A. and O.C.-F. conceived and designed the study. P.R., R.M.O. and U.A. performed the atomistic simulations. R.M.O., U.A. and O.C.-F. analysed the data. All authors contributed to writing the manuscript.

Competing interests

The authors declare no competing interests.

Additional information

Supplementary information is available for this paper at <https://doi.org/10.1038/s42005-020-0296-4>.

Correspondence and requests for materials should be addressed to R.M.O.

Reprints and permission information is available at <http://www.nature.com/reprints>

Publisher's note Springer Nature remains neutral with regard to jurisdictional claims in published maps and institutional affiliations.



Open Access This article is licensed under a Creative Commons Attribution 4.0 International License, which permits use, sharing, adaptation, distribution and reproduction in any medium or format, as long as you give appropriate credit to the original author(s) and the source, provide a link to the Creative Commons license, and indicate if changes were made. The images or other third party material in this article are included in the article's Creative Commons license, unless indicated otherwise in a credit line to the material. If material is not included in the article's Creative Commons license and your intended use is not permitted by statutory regulation or exceeds the permitted use, you will need to obtain permission directly from the copyright holder. To view a copy of this license, visit <http://creativecommons.org/licenses/by/4.0/>.

© The Author(s) 2020